Available online at www.sciencedirect.com
SCIENCE DIRECT®
International Journal of Heat and Mass Transfer 47 (2004) 1799–1816
International Journal of HEAT and MASS TRANSFER
www.elsevier.com/locate/ijhmt

Thermal conductivity decomposition and analysis using molecular dynamics simulations Part II. Complex silica structures

A.J.H. McGaughey, M. Kaviany *

Department of Mechanical Engineering, University of Michigan, 2250 G.G. Brown Laboratory, 2350 Hayward Street, Ann Arbor, MI 48109-2125, USA

Received 10 February 2003; received in revised form 13 October 2003

Abstract

Using molecular dynamics simulations, the thermal conductivity of silica-based crystals is found to be a result of two independent thermal transport mechanisms associated with atomic structure. The first mechanism is temperature independent, produces a thermal conductivity on the order of 1 W/m K, and is related to short length scale behavior. It is governed by the silicon coordination, which is unique to a given structure. The second mechanism is temperature dependent and is related to long length scale behavior. At a temperature of 300 K, the associated thermal conductivity ranges from 9 W/m K for the *c*-direction of quartz to 0.4 W/m K for zeolite-A. This mechanism is controlled by the atomic bond lengths and angles. Complex unit cells, notably cage structures, can distort the SiO_4 tetrahedra, leading to a shortening of the phonon mean free path and a spatial localization of energy. The results suggest that an alternative to the available minimum thermal conductivity model for amorphous materials is needed for the crystalline state.

1. Introduction

The porous crystals are a diverse group of materials characterized by large unit cells and Angstrom sized pores and channels. Among these are the zeolites [1], skutterudites [2], fullerenes [3], and metal organic frameworks [4,5]. The size of the pores is on the same scale as the dimensions of many atoms and molecules, leading to the use of porous crystals as molecular sieves and catalysts, and for gas storage applications. They typically have thermal conductivities on the order of 1–10 W/m K, with reported values as low as 0.4 W/m K [6,7]. Only recently has the systematic design of porous crystals begun to be realized [8,9]. Current efforts are geared towards molecular transport and storage applications. There is also interest in the design of porous crystals with very low thermal conductivities for applications as rigid insulators and to protect stored gases from ambient temperature fluctuations. As a first step towards design for thermal properties, the mechanisms by which heat is transferred in these materials must be understood. Here, this goal is pursued in the context of the zeolites.

The zeolites are a subset of the silica structures, materials built from SiO_4 tetrahedra. While there has been a considerable amount of experimental and theoretical work done to investigate the structure of zeolites and the transport of molecules through them [10–12], there has been little done to describe the nature of the thermal transport in these materials. They are generally synthesized as powders of micron sized crystals (to minimize the length of diffusion paths in transport applications), from which it is difficult to extract bulk phase properties. Even then, it is often only possible to make single crystals with sub-millimeter dimensions, making direct property measurements difficult. Challenges in the theoretical analysis of zeolites are centered around the complex unit cells, which can contain hundreds of atoms. Thermal transport mechanisms over a number of length scales must be resolved.

* Corresponding author. Tel.: +1-734-936-0402; fax: +1-734-647-3170.
E-mail address: kaviany@umich.edu (M. Kaviany).

0017-9310/$ - see front matter © 2003 Elsevier Ltd. All rights reserved.
doi:10.1016/j.ijheatmasstransfer.2003.11.009

Nomenclature

A	constant, BKS potential parameter
b, c	BKS potential parameter
B	constant
E	energy (kinetic and potential)
k_B	Boltzmann constant, 1.3806×10^{-23} J/K
k	thermal conductivity
L	simulation cell linear dimension
N	number of atoms
q	atomic charge
$\mathbf{q}$	heat current vector
r	inter-particle separation
t	time
T	temperature, K
U	potential energy
V	volume

Greek symbols

α	Wolf method parameter
ϵ	energy scale
ρ	density
σ	length scale
τ	time constant
ω	angular frequency

Subscripts

ac	acoustic
CP	Cahill–Pohl
i, j	summation index, particle label
lg	long range
nn	nearest neighbor
o	self (referring to a particle or cage)
op	optical
sh	short range

In dielectric solids (e.g., the silica structures), heat transfer is realized through the transport of phonons, quanta of energy associated with lattice vibrations. Many of the tools available for modeling heat transfer in such materials at the atomic level, such as the Boltzmann transport equation (BTE) and kinetic theory, rely on calculations done in the normal mode (phonon) coordinate space. The models often require the predictions to be fit to experimental data and are thus of limited use for new or complex materials. We note two recent phonon-based approaches that do not require the use of fitting parameters: (1) Omini and Sparavigna [13,14] have developed methods by which the lattice thermal conductivity can be predicted using an iterative solution of the BTE and detailed knowledge of the phonon dispersion. The calculations are formidable in terms of complexity and required computation time, but produce good agreement with experimental data. (2) McGaughey and Kaviany [15] have used phonon dispersion relations and relaxation times predicted from molecular dynamics (MD) simulations to predict the thermal conductivity of the face centered cubic (fcc) Lennard-Jones (LJ) argon crystal within the BTE single mode relaxation time formulation. While significant computation time is required, the implementation of this method into an existing MD code is straightforward. Good agreement is found with predictions from the MD simulations based on the Green–Kubo method.

While the modeling of a system as a set of harmonic (or anharmonic) oscillators (i.e., phonons) simplifies analyses, it also makes it difficult to relate the results back to the real coordinates of the system (i.e., the positions of the atoms). In trying to link design and analysis at the atomic level, it becomes apparent that the major difficulty is that design is done in real space, while analysis is done in phonon space. To proceed, one must either move the analysis to real space, or the design to phonon space.

Molecular dynamics simulations are an ideal tool for pursuing the analysis in real space. In Part I of this series of two papers [16], a method has been presented by which MD can be used to understand how the structure and thermal transport in simple LJ argon systems are related. Here, in Part II, the analysis techniques are extended to the silica structures. The range of materials available allows for further elucidation of the relationship between atomic structure and thermal conductivity.

The silica structures and the MD procedures are described. The thermal conductivity decomposition introduced in Part I is extended to include optical phonons, which result from the multi-atom unit cells. Using energy correlation functions, the geometry of the crystal structures, and dynamical data from the simulations, the thermal conductivity trends within and between the structures are examined. Two independent mechanisms that limit the thermal conductivity are identified, and used to propose structural metrics for the design of new, low thermal conductivity materials.

2. Silica structures

Molecular dynamics simulations of quartz, amorphous silica, and the zeolites sodalite (SOD), faujasite (FAU) and zeolite-A (LTA) have been performed. Initial coordinates for the crystal structures are taken from

Wycoff [17]. Typically, the zeolite frameworks contain aluminum atoms in place of some of the silicon atoms, and the structures are filled with non-framework anions and diffusing species such as water. Here, the focus is on all silicon–oxygen frameworks, also known as siliceous zeolites. All of the structures, which are built from SiO_4 tetrahedra, are shown in Fig. 1.

One length scale up from the SiO_4 tetrahedron, zeolites can be described by secondary building units (SBUs), which are named based on their geometry. For example, a 6R SBU is a ring structure made from six oxygen atoms and six silicon atoms. The three zeolites studied are built from the sodalite cage, which can be constructed with 4R and 6R SBUs. In SOD, the sodalite cages are directly joined on the 4R rings to form a cubic arrangement of cages. In FAU, the sodalite cages are joined by oxygen bridges on the 6R rings, resulting in a diamond arrangement of cages. LTA is a cubic arrangement of sodalite cages joined by oxygen bridges on the 4R rings. The atoms in each of the silica structures have a unique environment. The structures can be characterized by the distortion of individual tetrahedra and by considering the number of independent paths that lead away from a given atom. Such geometric descriptions will be used in the subsequent thermal conductivity analysis.

3. Simulation procedures

Other than as noted in this section, the simulation procedures are the same as those used in Part I for LJ argon. Some points are repeated for clarity.

The atomic interactions are modeled with the van Beest–Kramer–van Santen (BKS) interatomic potential [18,19], where the potential energy U_{ij} between atoms i and j is given by

$$U_{ij} = \frac{q_i q_j}{r_{ij}} + A_{ij}\exp(-b_{ij}r_{ij}) - \frac{c_{ij}}{r_{ij}^6}, \tag{1}$$

where q is an atomic charge, A, b, and c are constants specified by the types of atoms i and j (either oxygen or silicon), and r_{ij} is the distance between atoms i and j. The BKS potential has been found to reproduce the static structure of dense silica phases well, although the predicted Si–O–Si angles in quartz are 6° larger than the experimental value. The agreement with the experimental dynamical properties (e.g., the infrared

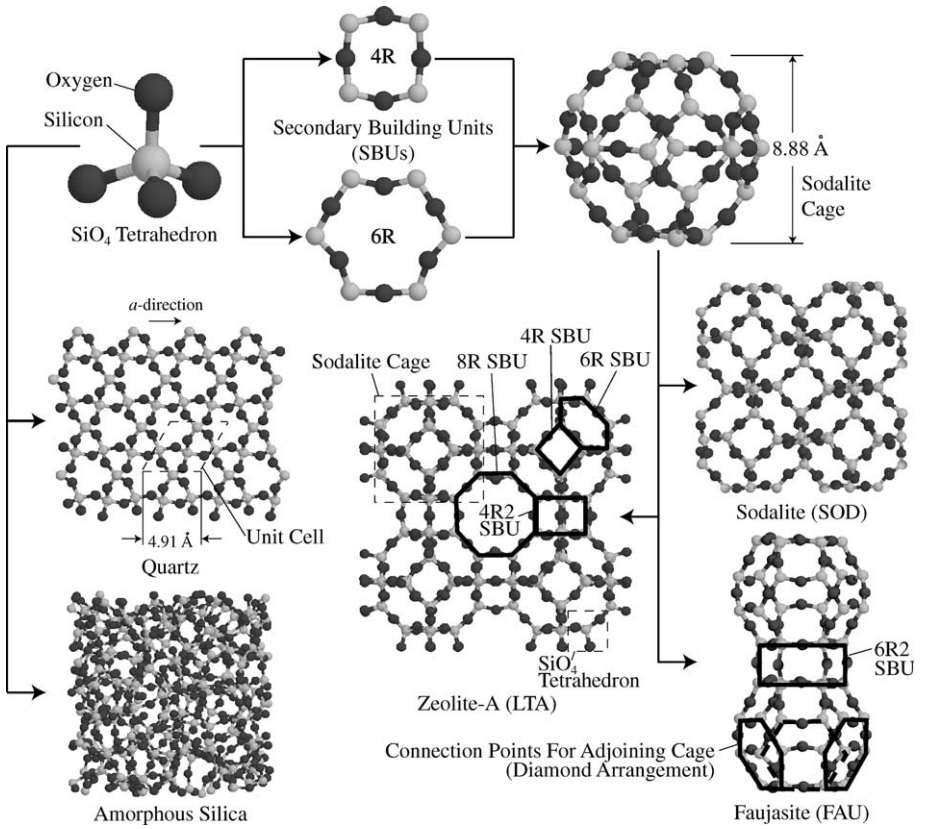

Fig. 1. Silica structure building blocks and materials studied in the MD simulations.

spectrum) is good at high frequencies, but decreases at lower frequencies [20]. The shortcomings of the BKS potential are most likely a result of its two-body nature, which cannot explicitly model the bond angles. While a three-body term would help in this regard, it would also significantly increase the required computation time, which is already long.

The electrostatic interactions are modeled using the Wolf method [21], where the first term in Eq. (1) is calculated as

$$\frac{q_i q_j}{r_{ij}} \simeq \frac{q_i q_j \mathrm{erfc}(\alpha r_{ij})}{r_{ij}}. \tag{2}$$

The use of the Wolf method instead of the traditional Ewald sum is advantageous in that it significantly reduces the required computation time. The Wolf method is essentially equivalent to ignoring the long range electrostatic interactions in the Ewald sum. The Wolf method is successful because it forces there to be zero net charge within the volume bounded by the cutoff radius. When the full Ewald sum was used in the current simulations, the long range force and energy contributions were on the order of one percent of the short range terms. This type of behavior has been reported previously, and is a result of a suitable selection of α [22,23]. The parameter α provides the damping necessary to make the electrostatic interaction short range and must be specified. Demontis et al. [24] suggest choosing a value of $4/L$, where L is the size of the simulation cell. They show that this value gives the closest agreement with the full Ewald sum for a range of crystals, including some zeolites. In the current simulations, a constant value of α is used so that the interatomic potential is the same for each of the materials. A value of 0.223 Å^{-1} is chosen, which corresponds to a typical $4/L$ for the SOD structure.

All reported data correspond to simulations in the *NVE* (constant mass, volume and energy) ensemble. The time step used is 0.905 fs (the smallest time scale of interest is on the order of 15 of these time steps) and the simulations are run at zero pressure. The temperatures considered are between 100 and 350 K in increments of 50 K. The interactions are truncated and shifted at a radius that is one half of the shortest side length of the simulation cell (which is cubic for all the materials except quartz), so as to include as many atoms as possible in the dynamics.

Specifics of the simulations for each of the four crystals are given in Table 1, including data specific to a temperature of 300 K. In the table, N is the number of atoms in the simulation cell and ρ is density. In the determination of the zero pressure cell size for quartz, the pressure was independently controlled in three orthogonal directions to allow for the proper relaxation of the non-cubic unit cell. For the zeolites and the amorphous phases, the ratio of the three side lengths was fixed at unity.

Table 1
Crystal structure parameters

Structure	Unit cell (Å)	Atoms/ unit cell	N	ρ (kg/m^3)
Quartz	4.91(a), 5.52(c)	9	576	2589
SOD	8.88	36	288	1705
FAU	24.72	576	576	1266
LTA	12.05	72	576	1368

Dimensions and density are at $T = 300$ K.

An amorphous silica phase is generated by heating the quartz crystal until it is a liquid, waiting until any memory of its initial configuration has been lost, and then quenching back to the solid phase. In the liquid state, the atoms can get very close together. The BKS potential is not able to handle the resulting interactions as it does not go to positive infinity as the atomic separation goes to zero for the Si–O and O–O pairs. To force this to happen, a 24-6 LJ potential is added to the BKS potential [25]. The implemented potential for amorphous silica is given by

$$U_{ij} = \frac{q_i q_j \mathrm{erfc}(\alpha r_{ij})}{r_{ij}} + A_{ij}\exp(-b_{ij} r_{ij}) - \frac{c_{ij}}{r_{ij}^6} + 4\epsilon_{ij}\left[\left(\frac{\sigma_{ij}}{r_{ij}}\right)^{24} - \left(\frac{\sigma_{ij}}{r_{ij}}\right)^{6}\right]. \tag{3}$$

The values of ϵ, an energy scale, and σ, a length scale, are taken from [25]. The effect of the new terms is minimal around and beyond the equilibrium separation distance. While use of the modified potential is crucial in the liquid phase, it is also important to use it in the resulting amorphous phase. There are often a few places in the structure where the atoms are close enough to need the extra terms to prevent non-physical behavior.

The nature of the MD quench has a significant effect on the final amorphous structure [26]. If it is too fast, many atoms may not have the proper coordination (two for oxygen and four for silicon). The density of amorphous silica at room temperature is 2220 kg/m^3 [27]. However, the potential functions available typically generate a structure in tension at a pressure of 2–3 GPa at this density. The equilibrium, zero pressure density found by relaxing from the experimental density is typically around 2350 kg/m^3 [28]. To be consistent with the crystal simulations, the zero pressure state is used here.

The following procedure is used to generate the amorphous phase. It is based on the recommendations of previous reports [26,29,30] and observations from the current investigation. The cell size is initially fixed so that the density is 2200 kg/m^3. A 576 atom sample of quartz is heated to a temperature of 10^4 K and run in the *NVT* (constant mass, volume and temperature) ensemble for 10^4 time steps. The system is then quenched at a rate

Table 2
Amorphous silica structure parameters

Structure	ρ (kg/m^3)	Si coordination (%)	O coordination (%)
AS1	2338	99.7	99.5
AS2	2326	99.5	99.5
AS3	2364	99.5	100

There are 576 atoms in each structure. The density is at zero pressure and $T = 300$ K.

of 3.63×10^{12} K/s to a temperature of 200 K (this corresponds to 2.98×10^{6} time steps). This length of time is required to establish a phase in which over 99% of the atoms consistently have the proper coordination. The system is then relaxed to the zero-pressure condition. Characteristics of three such amorphous phases are given in Table 2. Thermal conductivities predicted from the three structures will be compared to check if they are truly disordered.

The thermal conductivity, k, is determined using the Green-Kubo approach, which predicts that for an isotropic material [31],

$$k = \frac{1}{k_B V T^2}\int_0^\infty \frac{\langle \mathbf{q}(t)\cdot\mathbf{q}(0)\rangle}{3}\,\mathrm{d}t, \tag{4}$$

where k_B is the Boltzmann constant, V is the volume of the simulation cell, T is temperature, $\mathbf{q}$ is the heat current vector, t is time, and $\langle \mathbf{q}(t)\cdot\mathbf{q}(0)\rangle$ is the heat current autocorrelation function (HCACF). This method relates the dissipation of thermal fluctuations in an equilibrium system to its thermal conductivity. Further detail is given in Section 2 of Part I. In quartz, which is anisotropic, the directionally dependent thermal conductivities are obtained by considering the appropriate components of the heat current vector, and then performing the autocorrelation. Due to the strongly covalent silicon-oxygen bonds, the electronic component of the thermal conductivity is assumed negligible.

Five independent simulations (differentiated by random initial velocities so as to get a good sampling of the associated phase space [32]) are performed for each temperature and structure of interest, and the HCACFs are averaged before proceeding with the analysis. For quartz at a temperature of 100 K, 10 independent simulations are necessary to obtain a good average due to the long convergence times in both the a- and c-directions.

4. Results and analysis

4.1. Heat current autocorrelation function

In the LJ fcc argon crystal the HCACF decays monotonically [16,33,34]. Small oscillations can be attributed to the periodic boundary conditions. In other materials, such as β-silicon carbide [32] and diamond [35], larger oscillations are present, but their magnitudes are small compared to the total value of the HCACF. In such cases, the thermal conductivity, which is related to the converged value of the integral of the HCACF through Eq. (4), can be specified using different approaches. These include a direct specification of the converged value of the integral, the first dip method [32], and the fit of the sum of two exponential functions to the HCACF and subsequent analytical integration [16,35].

The HCACFs of the silica structures do not decay monotonically. As shown in Fig. 2(a) and (b), for quartz(a) and quartz(c) at temperatures of 250 and 200 K, respectively, there are large oscillations in the HCACF. Similar oscillations have been attributed to the relative motion of bonded atoms with different masses [35]. However, such behavior has also been observed in an all germanium clathrate structure [36]. This suggests the more general explanation that the oscillations are a result of optical phonons. The first dip and exponential fit methods are not suitable for determining the thermal conductivity. Even the direct specification of the integral in Eq. (4) is not trivial. Noise in the HCACF can result in no obvious convergence region.

We propose the following scheme for the direct specification of the thermal conductivity. First, the integral is averaged in overlapping blocks of 2500 time steps. The resulting curves related to Fig. 2(a) and (b) are shown in Fig. 2(c) and (d), along with the raw data. When the convergence is clear [Fig. 2(c)], a region of at least 5000 time steps is chosen over which the integral is deemed to have a constant value. The integral is averaged over this region, and this value is used to determine the thermal conductivity. When the convergence is not clear [Fig. 2(d)], we have observed that the oscillations reach a minimum (i.e., a neck) before the divergence begins. Through comparison to the cases where the integral clearly converges, it is found that the HCACF function beyond this point does not make a significant contribution to the integral. An average of the integral is taken over 1000 time steps around the neck, and this is the value used in the specification of the thermal conductivity.

4.2. Thermal conductivity decomposition

Consistent results have been obtained using the direct specification method for predicting the thermal conductivity. To allow for further analysis, the thermal conductivity decomposition described in Part I is now extended to the silica structures.

The HCACF of the silica structures cannot be fitted with the sum of two exponential decays as used for the LJ argon fcc crystal. The oscillations in the HCACF suggest that looking at its Fourier transform may help in extending the model. There are between four and ten well defined peaks in the HCACF spectra of the four crystals (not shown). The peak locations are in the

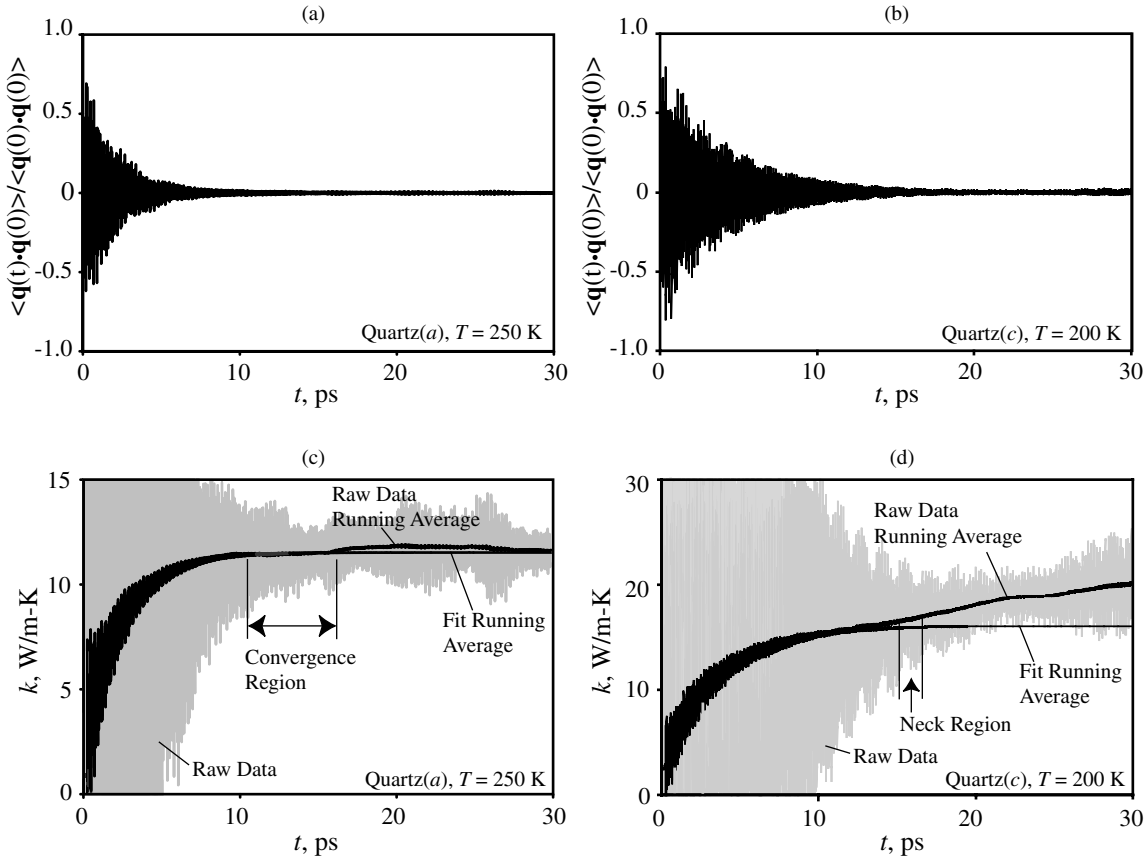

Fig. 2. Time dependence of the HCACF [(a) and (b)] and its integral [(c) and (d)] (whose converged value is the thermal conductivity) for quartz(a) at $T = 250$ K and quartz(c) at $T = 200$ K.

infrared region of the electromagnetic spectrum. Based on phonon dispersion curves calculated from the zero temperature configuration of the four crystals (not shown), the peak frequencies correspond to optical phonons. For each structure, the spectrum is similar to the infrared spectrum determined from MD (which is related to the dipole moment). This is likely due to the strong contribution of the electrostatic term in the force and energy calculations in the heat current [see Eq. (6) of Part I]. There are more optical phonon modes than peaks for all four crystals, which indicates that it is only the infrared active modes that contribute to the thermal conductivity. The spectra are also in qualitative agreement with the infrared spectra found for zeolites in previous MD simulations [37,38]. There are some discrepancies in the peak heights and locations, which may be a result of the different interatomic potentials used. A significant amount of research has been done to relate the infrared spectra of zeolites to their structural features (i.e., bond lengths, angles, SBUs, etc.) [38–41]. While some general guidelines have been suggested, no definitive interpretations of the spectra have been established.

Based on these observations and the results of Part I, the HCACF for the silica crystals is decomposed as

$$\frac{\langle \mathbf{q}(t)\cdot\mathbf{q}(0)\rangle}{3} = A_{\mathrm{ac,sh}}\exp(-t/\tau_{\mathrm{ac,sh}}) + A_{\mathrm{ac,lg}}\exp(-t/\tau_{\mathrm{ac,lg}}) + \sum_i B_{\mathrm{op},i}\exp(-t/\tau_{\mathrm{op},i})\cos(\omega_{\mathrm{op},i}t), \quad (5)$$

so that, from Eq. (4)

$$k = \frac{1}{k_{\mathrm{B}}VT^2}\left(A_{\mathrm{ac,sh}}\tau_{\mathrm{ac,sh}} + A_{\mathrm{ac,lg}}\tau_{\mathrm{ac,lg}} + \sum_i \frac{B_{\mathrm{op},i}\tau_{\mathrm{op},i}}{1+\tau_{\mathrm{op},i}^2\omega_{\mathrm{op},i}^2}\right) \equiv k_{\mathrm{ac,sh}} + k_{\mathrm{ac,lg}} + k_{\mathrm{op}}. \quad (6)$$

The τ terms are time constants and the A and B coefficients represent the strength of a given mode. The subscripts ac, sh, lg, and op refer to acoustic, short range, long range, and optical, respectively. This procedure is not suitable for the amorphous phase, where there are

no sharp peaks in the HCACF spectra. Its thermal conductivity is specified directly from the integral of the HCACF.

The decomposition is the same as equations (15) and (16) of Part I, with the addition of the third term, which accounts for the optical phonons with exponentially decaying sinusoids. The summation in the third term is over the peaks in the HCACF spectrum at angular frequency ω. As described in Part I, the first term, $k_{ac,sh}$, corresponds to short wavelength acoustic phonons with mean free paths equal to one half of their wavelength. This is the minimum value of the mean free path as described in the Cahill–Pohl (CP) high scatter limit [42,43], discussed in Section 1 of Part I. The time constant $\tau_{ac,sh}$ indicates how long it takes energy to transfer from an atom to a nearest neighbor atom. The second term, $k_{ac,lg}$, which we have associated with acoustic phonons with longer mean free paths, has a longer time constant.

The fitting of the sum of two exponential decays to the LJ argon fcc crystal HCACF is a straightforward task using a mathematical software package such as Mathematica (used here for all calculations). The task of fitting the silica HCACFs to a function of the form of Eq. (5), which requires up to 34 unknowns (for the case of FAU), is not trivial. The general procedure is outlined next.

The terms in the optical summation are individually fitted using the imaginary part of the Fourier transform of the HCACF. Overlapping peaks are fitted together. Visually, the total optical component gives an excellent fit to the raw HCACF in the time domain. When the fit is subtracted from the raw data, the remaining signal appears to be noise. It is not until the integration of Eq. (4) is performed that the behavior represented by the first two terms of Eq. (5) becomes apparent. The fit of the short and long range acoustic modes is made on the integral. The appropriate function is found by integrating Eq. (5) to a limit of t as opposed to infinity. The fitting algorithm requires initial guesses for each parameter. Different choices for $A_{ac,sh}$ and $\tau_{ac,sh}$ result in a consistent value of $A_{ac,sh}\tau_{ac,sh}$ [as found in Eq. (6)], but do not give unique values for the individual parameters. This occurs because the value of $\tau_{ac,sh}$ is small and $A_{ac,sh}/B_{op,i}$ is of order 0.01, so that $A_{ac,sh}$ is on the same order as the noise in the HCACF after the optical fit has been subtracted. To specify $\tau_{ac,sh}$, the energy correlation analysis described in Section 4.2 of Part I is used. The values obtained are around 0.015 ps. This is smaller than the values near 0.26 ps found for the LJ argon structures, and is a result of the higher frequencies available to phonons in the silica structures. There is no difficulty in the specification of $A_{ac,lg}$ and $\tau_{ac,lg}$. The fit integral is shown in Fig. 2(c) and (d). The results for the decomposition of the quartz(a) HCACF at a temperature of 250 K are given in Table 3.

Table 3
Thermal conductivity decomposition for quartz(a) at $T = 250$ K

Component	τ (ps)	$\omega/2\pi$ (THz)	k (W/m K)
Short range acoustic	0.016	–	**1.143**
Long range acoustic	2.37	–	**9.494**
Optical			
1	3.19	14.2	0.087
2	1.65	18.3	0.436
3	2.50	21.6	0.052
4	1.24	22.8	0.242
5	2.82	32.8	0.070
			0.887
Total			**11.524**

The time constant for the short range acoustic phonon component is obtained from the energy correlation analysis.

The thermal conductivities predicted by the decomposition of Eq. (6) and the values obtained from the direct specification of the integral agree to within 5% for all cases considered except quartz(c) at 100 K (−13.8%), FAU at 100 K (+8.7%), and LTA at 100 K (+15.6%) and 150 K (+9.7%). These cases all correspond to low temperatures, where long convergence times can make the direct specification of the integral ambiguous, even when using the methods described in Section 4.1. Based on these results, the error in the thermal conductivity predictions is taken as ±5%.

4.3. Thermal conductivity results

In Fig. 3(a), the predicted thermal conductivities of the four crystals are plotted as a function of temperature. Only quartz data in the c-direction are shown. Least squares power law fits are added for the three zeolites to guide the eye. Also shown are experimental data for quartz(c) and amorphous silica [44], and the predictions of the CP high scatter limit for amorphous silica. As discussed in Section 5.2.4 of Part I, the CP limit is a quantum model, while the MD simulations are classical. In Fig. 3(a), the quantum formulation of the CP limit is plotted to allow for comparison with the experimental amorphous silica data. All numerical data [including quartz(a)] are given in Table 4.

The predicted quartz(c) thermal conductivities are within ±25% of the experimental values. The quartz(a) results over predict the experimental data by an average of 40%. This is a good result for an MD simulation, and gives confidence to the use of the BKS potential for modelling thermal transport in silica structures. The CP limit falls below all of the experimental and MD results.

There is minimal experimental or computational data available for zeolite thermal conductivity. Murashov [45]

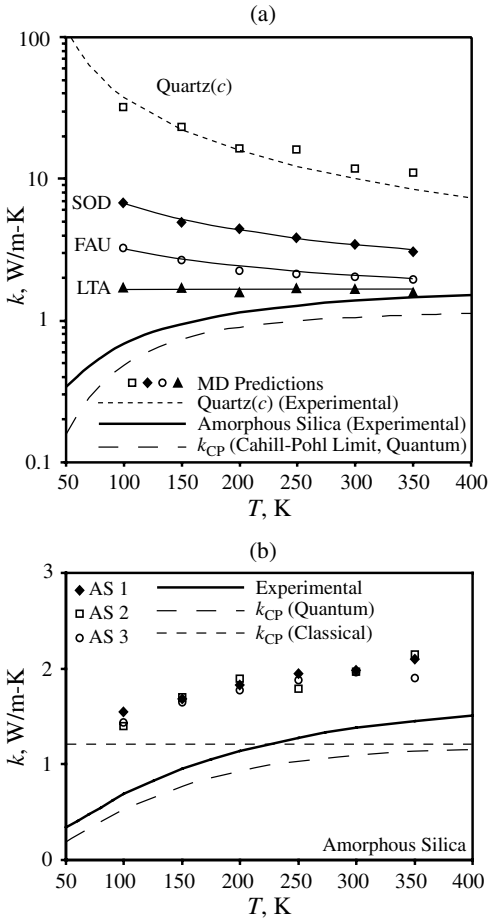

Fig. 3. Molecular dynamics predicted and experimental thermal conductivities plotted as a function of temperature for: (a) silica crystals and (b) amorphous silica. All of the structures are shown in Fig. 1. The zeolite MD data are joined by best fit power law curves to guide the eye.

has predicted the thermal conductivity of LTA and FAU using the BKS potential and a non-equilibrium MD method. There is significant scatter in the limited results, suggesting that not enough data were generated to give a good statistical average. The current MD calculations for LTA are in reasonable agreement with Murashov's results, while our FAU values are higher. Griesinger et al. [46] have measured the effective thermal conductivity of zeolite powders with various filling gases. For zeolite NaA (the LTA structure with some aluminum atoms replacing the silicon atoms in the cages and guest sodium atoms), fitting the experimental data with a network model gives a bulk thermal conductivity of 3.3 W/m K at a temperature of 423 K.

The predicted thermal conductivities for the three amorphous phases are shown in Fig. 3(b), along with the experimental data [44] and the CP limit (both the quantum and classical forms are shown). In the CP limit calculations, the density and speed of sound are taken from the experimental data, and assumed to be independent of temperature for both curves. For the classical curve, the specific heat is taken as the classical harmonic value. The variation due to anharmonicities in the MD simulations is found to be only a few percent over the temperature range studied.

The agreement of the thermal conductivities of the three MD amorphous silica phases is good, indicating that the simulation cells are fully disordered. Thermal conductivity predictions for the amorphous phase at the experimental density (not shown) were not distinguishable from those given here within the numerical uncertainty. Further discussions and calculations will use an average of the results unless noted. The amorphous silica predictions are 40–110% higher than the experimental data. The temperature trend is the same, and the agreement improves as the temperature is increased. Using a direct application of the Fourier Law of heat conduction in an MD simulation (known as the direct method, see Section 2 of Part I) with the BKS potential, Jund and Jullien [30] have predicted the thermal conductivity of amorphous silica. In the temperature range of 100–400 K, their results agree with experimental data to within ±20%. Based on the results of Part I for amorphous LJ argon, no size effects are expected for the amorphous silica phase. Jund and Jullien did not consider any size effects in their predictions, which are generally important in the application of the direct method, and lead to an underprediction of the thermal conductivity. Thus, had Jund and Jullien included size effects, it is possible that their predictions would come into agreement with ours, indicating that the BKS potential is only somewhat suitable for modeling of the amorphous silica phase.

The temperature dependence of the amorphous phase thermal conductivity is often associated with the temperature dependence of the specific heat, which is a quantum effect (in the classical, harmonic limit the specific heat is constant). However, as found here and by others [30,47], classical MD simulations of amorphous materials, where the specific heat is approximately constant, generate temperature dependent thermal conductivities. This surprising result, which indicates that the positive temperature dependence of the amorphous silica phase thermal conductivity is not purely a quantum effect, warrants further investigations. It has been suggested that the positive temperature dependence is a result of the coupling of anharmonicity and disorder [48,49]. The description of amorphous phase lattice vibrations in terms of diffusons, locons, and propagons, as suggested by Allen et al. [50], may be a suitable place to start.

The absolute value and temperature dependence of the thermal conductivities decrease from quartz to SOD

Table 4
The predicted thermal conductivities from the MD simulations

Structure T (K)	Quartz(c/a)	SOD k (W/m K)	FAU	LTA	AS
100	31.2/27.5	6.82	3.29	1.72	1.46
	[39/20.8]		[1.4]	[1.2]	[0.7]
150	23.2/17.4	5.02	2.71	1.70	1.67
	[23.1/13]				[1.0]
200	16.2/13.2	4.49	2.28	1.58	1.83
	[16.4/9.5]		[1.3]	[1.5]	[1.1]
250	15.7/11.5	3.91	2.18	1.66	1.87
	[12.7/7.5]				[1.3]
300	11.7/8.6	3.53	2.07	1.68	1.96
	[10.4/6.2]		[0.6]	[1.3]	[1.4]
350	10.8/8.10	3.09	2.00	1.61	2.04
	[8.8/5.3]				[1.4]

The numbers in square brackets under the quartz and amorphous silica data correspond to experimental values from Ref. [44]. The numbers in square brackets under the FAU and LTA data are the MD results from [45]. Those simulations also predict quartz thermal conductivities of 16/8.2 W/m K at $T = 300$ K.

to FAU to LTA. The introduction of lattice pores has reduced not only the thermal conductivity, but also its temperature dependence. The same phenomenon has been observed in germanium-based structures [36]. Both directions for quartz, SOD, and FAU show the expected decrease in the thermal conductivity above one-tenth of the Debye temperature [51], which for quartz is 290 K [52]. We assume that the zeolites have a comparable value. For LTA, all of the calculated thermal conductivities are within a range of 0.14 W/m K, which approaches the resolution of the predictions. A slight decrease in the thermal conductivity over the temperature range considered is discernable.

A possible interpretation of the decreasing temperature dependence of the thermal conductivity of the crystal structures is that the thermal transport mechanism is changing to that which exists in the amorphous phase (i.e., the mean free path of all phonons is approaching its minimum value). However, it appears as though the crystal curves are approaching a temperature independence, and it is unclear if a transition to a positive temperature dependence will occur. Thus, the effect of a high phonon scattering rate (a short mean free path) appears to be different in the crystalline and amorphous phases. This point will be further addressed in Section 4.4.

The thermal conductivity trend between the structures can be qualitatively interpreted in terms of the overall stiffness of each one. With its high density, quartz will be the stiffest. For the zeolites, consideration of the joining mechanisms between the sodalite cages suggests that SOD (where the cages are directly attached) will be the stiffest, followed by FAU (where the oxygen bridges contain six elements), and then by LTA (where the oxygen bridges contain four elements). The thermal conductivities are consistent with this explanation.

In Fig. 4(a)–(d), the decompositions of the thermal conductivities of quartz(c), SOD, FAU, and LTA, based on Eq. (6), are shown. For all cases, both the optical phonon and short range acoustic phonon contributions are of order 1 W/m K and independent of temperature. This temperature independence has been noted for the short range acoustic phonon modes in LJ argon [16,34]. For each structure, the optical contribution falls within a range of ±0.08 W/m K, while the short range acoustic phonon contribution falls within a range of ±0.18 W/m K. The only exceptions to this are the short range acoustic phonon modes for quartz(c) at temperatures of 100 and 150 K. Here, the short range acoustic phonon mode contribution is 0.5 W/m K lower than at the higher temperatures. We attribute this discrepancy to the difficulty in performing the fit of the HCACF when the thermal conductivity is high ($k_{ac,sh}/k$ is of order 0.05 in these two cases).

Che et al. [35] studied diamond at a temperature of 300 K over a range of simulation cell sizes, using a model containing our $k_{ac,sh}$ and $k_{ac,lg}$ terms. The total thermal conductivity is found to be 1200 W/m K (the experimental value is 2300 W/m K). Their term corresponding to our $k_{ac,sh}$ is independent of the simulation cell size, and equal to 1.8 W/m K. This is the same order as $k_{ac,sh}$ in the silica structures. No effects along the lines of our k_{op} are evident (i.e., large oscillations in the HCACF), even though the diamond structure has optical phonons. Based on our observation of k_{op} being of order 1 W/m K, not including this was justified in their case. However, when the total thermal conductivity is on the order of 1 W/m K, as with the zeolites, the optical phonon contribution cannot be ignored.

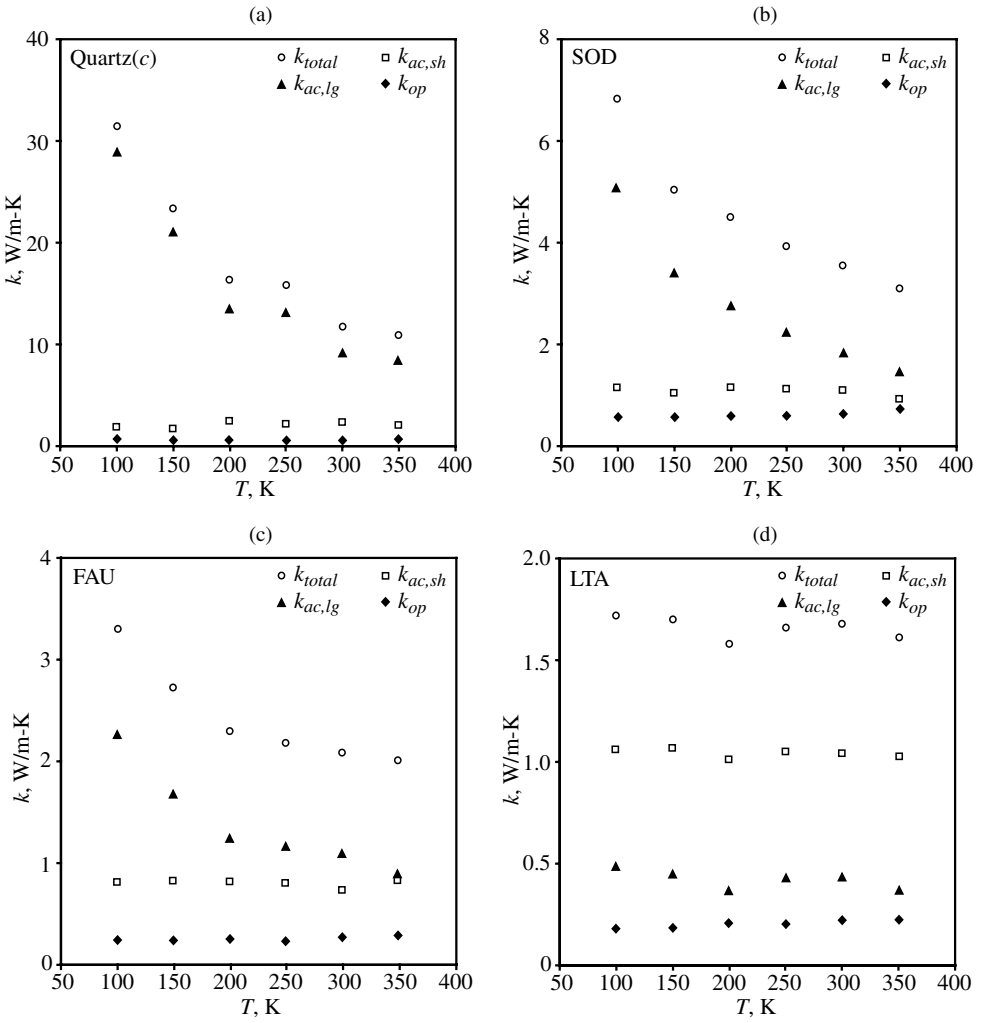

Fig. 4. Thermal conductivity decomposition according to Eq. (6) for: (a) quartz(*c*); (b) SOD; (c) FAU, and (d) LTA.

The magnitude and temperature dependencies of the thermal conductivities of the four crystals are primarily differentiated by the $k_{ac,lg}$ term. From the trends shown in Fig. 4, it appears as though the long range acoustic phonon modes are being inhibited in the zeolites (i.e., the mean free path of all phonons is approaching the limiting value of one half wavelength). The associated time constants, $\tau_{ac,lg}$, for the four crystals are of the same order at a given temperature, and are thus not enough to distinguish the wide range of $k_{ac,lg}$. The crystal structure must be taken into account to explain the trends.

4.4. Thermal conductivity limits in crystals

Low thermal conductivity in silica structures is achieved by reducing the phonon mean free path. This can be accomplished in three ways: increasing the temperature [seen in Fig. 3(a)], introducing disorder (as found in the amorphous phase), or by creating a crystal structure that scatters phonons over a short length scale. It is the last mechanism that is present in the zeolites, and this is explored in the next two sections. The effects of disorder and crystal structure are shown in Fig. 5(a), where MD predicted and experimental thermal conductivities of silica structures at a temperature of 300 K are plotted as a function of their densities. The density is limited by the requirement of a stable crystal structure. For the zeolites, FAU is the most open framework possible. Further reduction in the thermal conductivity requires breaking the lattice periodicity (e.g., with defects or imperfections) or the introduction of bulk porosity (e.g., silica aerogel). There will be an accompanying loss in strength and lattice periodicity, which may make such materials undesirable.

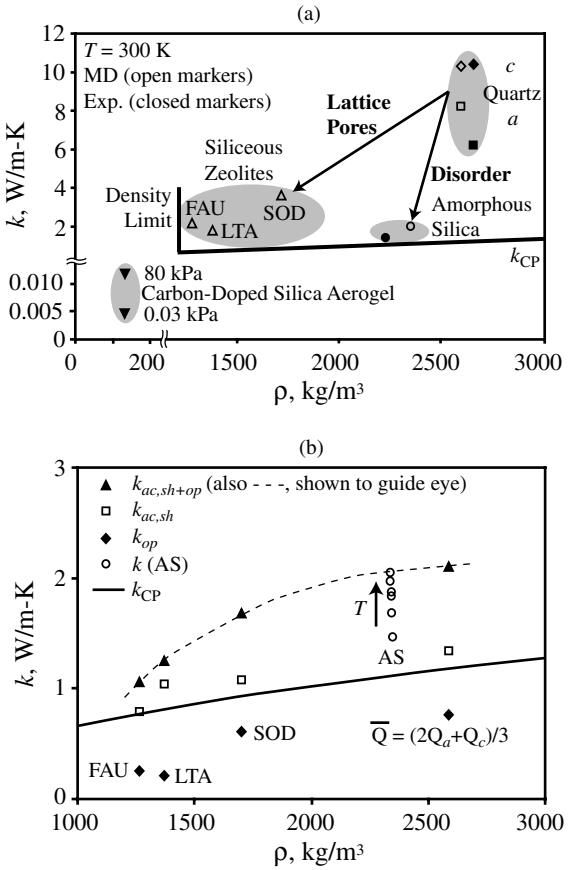

Fig. 5. (a) Molecular dynamics and experimental thermal conductivities of silica structures plotted against density at $T = 300$ K. Limits imposed by structural stability and disorder are shown. (b) The temperature independent $k_{ac,sh}$ and k_{op} contributions to the thermal conductivity plotted against the $T = 300$ K density. Also included are the MD amorphous silica results and the CP limit. In both (a) and (b) the CP limit is the quantum formulation calculated with a density independent speed of sound (the experimental value).

Optical phonon modes typically have close to flat dispersion curves and therefore, low group velocities. Thus, while the time constants of the optical phonon modes in the thermal conductivity decomposition are longer than that of the short range acoustic phonons, the distance over which they are effective may be comparable. The temperature independence of both of these components suggests that they should be considered together. When the sum of $k_{ac,sh}$ and k_{op} (referred to hereafter as $k_{ac,sh+op}$) is calculated for each of the crystals, the values obtained increase with increasing density, and are consistent with the scale of the amorphous phase predictions at higher temperatures. Temperature averaged thermal conductivity results are plotted against the density at a temperature of 300 K in Fig. 5(b). Also shown are the amorphous silica results and the CP limit under the assumption of a density independent speed of sound. The quartz values correspond to an average of the *c*-direction value and twice the *a*-direction value. The $k_{ac,sh}$ values are close to the thermal conductivities predicted by the CP limit, supporting the equivalence of the two terms as suggested in Section 5.2 of Part I. The inclusion of k_{op} gives a significantly higher value than k_{CP}. Note that the trend in the $k_{ac,sh+op}$ values is not the same as the total thermal conductivity trend (LTA has a higher density than FAU, but a lower total thermal conductivity).

To further understand the $k_{ac,sh+op}$ trend, the crystal structure of the five materials can be investigated using the concept of the coordination sequence (CS) [53]. The CS of a material describes the environment seen by one of its constituent atoms. For silica structures, only the silicon atoms are considered. For each of the crystals, each silicon atom is equivalent to all others within that structure. The first three terms in the CS for the five silica structures are given in Table 5. For quartz, the CS is 4–12–30. This means that each silicon atom has four nearest neighbor silicon atoms. The total number of distinct neighbors of those four atoms (not including any double counting of atoms from previous stages) is twelve, and so on. The amorphous result is based on structure 1 (see Table 2) and takes an average of the CS of each silicon atom. The fact that the first term is 3.99 results from not all the atoms having the proper coordination (see Table 2).

The trend in the CSs towards fewer neighbors is consistent with the $k_{ac,sh+op}$ trend. In Part I, it was found that the $k_{ac,sh}$ value for the fcc LJ argon crystal does not change over a large density range (see Table 1 of Part I). The analysis here explains why this is so. It is not the density that affects this component of the thermal conductivity, but the crystal structure, which for argon was always an fcc crystal. Thus, while the value of the time constant $\tau_{ac,sh}$ changes with the density (which affects the nearest neighbor separation), $k_{ac,sh}$ remains constant because there are always 12 nearest neighbors.

At the higher temperatures, the amorphous results qualitatively fit the CS trend. However, there is a temperature dependence not seen in the crystals. The question then arises of how to resolve the temperature dependence of the amorphous data with the temperature independence of the $k_{ac,sh+op}$ terms. What these results suggest is that the mechanisms limiting thermal transport in the crystal phase are not the same as those in the amorphous phase. That being said, the CP limit may not be a suitable tool for modeling the lower limits of thermal conductivity in crystals. While it is able to capture the temperature dependence and magnitude of amorphous results, it is not able to capture what we have identified as structure dependent limits in crystals, or the effect of optical phonons. To formulate a crystalline

Table 5
A number of different comparisons between the structures

Structure	Quartz(c/a)	SOD	FAU	LTA	AS
k (W/m K)	16.2/13.2	4.49	2.28	1.58	1.83
$k_{ac,lg}$ (W/m K)	13.4/11.5	2.75	1.23	0.37	–
$k_{ac,sh+op}$ (W/m K)	3.36/1.93	1.73	1.05	1.21	–
$\tau_{ac,lg}$ (ps)	3.59/2.63	1.67	3.22	1.49	–
Coordination sequence	4–12–30	4–10–20	4–9–16	4–9–17	3.99–11.3–25.2
τ_{cage} (ps)	–	0.67	1.35	1.72	–
Spread of Si–O bond lengths in equilibrium tetrahedron (Å)	–	0	0.017	0.026	–
Mean deviation of O–Si–O angles in equilibrium tetrahedron (°)	–	3.6	2.1	1.7	–

Temperature dependent data at $T = 200$ K.

minimum thermal conductivity model, specific details about the structure must be considered (e.g., the CS). The atomic species present will also be important, as is evident from the result that the $k_{ac,sh}$ value for argon is of order 0.1 W/m K, compared to order 1 W/m K for the silica structures.

The concept of the short length scale behavior representing a thermal conductivity limit can be further investigated by considering the MD results of Li et al. [32] for β-silicon carbide. The introduction of point defects to the system results in a faster decay of the HCACF, and a significantly lower, temperature independent thermal conductivity. This is consistent with a reduction in $k_{ac,lg}$, as observed in the current simulations as a result of the cage structure of the unit cells. In the work of Li et al., it is a result of the loss of periodicity that is brought about by defects. In both cases, what remains is a temperature independent thermal conductivity. Similar results related to defects have been found in MD studies of diamond [35] and yttria-stabilized zirconia [54].

The results of this section have allowed for an interpretation of the relative magnitudes of the $k_{ac,sh}$ and k_{op} components of the thermal conductivity. However, the mechanism by which long range effects in the zeolites are inhibited (i.e., the large reduction in $k_{ac,lg}$ compared to quartz) has not been addressed. This is considered next.

4.5. Atomic structure and thermal conductivity

In Part I, the time constant $\tau_{ac,lg}$ was associated with acoustic phonons with a mean free paths greater than one half of their wavelength. In argon, the values of $\tau_{ac,lg}$ were consistent with the temperature trend of $k_{ac,lg}$. While this holds within each of the silica crystals, it is not sufficient to understand the trends between structures at a given temperature (i.e., the $\tau_{ac,lg}$ time constants are not consistent with the $k_{ac,lg}$ values between structures, as given in Table 5 at a temperature of 200 K). To explain this phenomenon, we believe that additional time scales, associated with the localization of energy on the sodalite cages in the zeolites, are being manifest in the HCACF. This idea is investigated in this section using a series of real-space (as opposed to phonon-space) analysis techniques. Note that we are not referring to localization in the context of a specific phonon mode (as is often discussed with respect to amorphous materials), but in the context of the overall spatial localization of energy that may result in a crystal structure that quickly scatters phonons.

Energy autocorrelations for the sodalite cages in the three zeolites have been formed. The normalized results for FAU are shown in Fig. 6(a). Along with the expected $\tau_{ac,sh}$ scale, which is present in all the energy correlations investigated, there is a clear secondary scale, shown as τ_{cage}. The value of τ_{cage} for the three zeolites, calculated based on an average over 8 ps, are given in Table 5. The increasing magnitude of τ_{cage} from SOD to FAU to LTA is consistent with the decreasing $k_{ac,lg}$ among these structures. We interpret this time scale as representing a localization of energy on the sodalite cages. It is this phenomenon that results in the zeolites having significantly lower thermal conductivities than quartz.

To gain further insight into the localization of energy on the sodalite cages, energy correlations between nearest neighbor silicon atoms in each of the structures are considered. In each of the quartz and SOD structures, all oxygen atoms have an equivalent environment, so that there is only one type of Si–Si pair. This is not the case for LTA and FAU, where there are distinct oxygen positions (3 and 4, respectively). These are shown in Fig. 7, where the distinct oxygen positions in each structure are identified by different colors. There is no order in the amorphous structure outside of a given tetrahedron.

The significant results of the energy correlations are given in Fig. 6(b) and (c). The curves are normalized

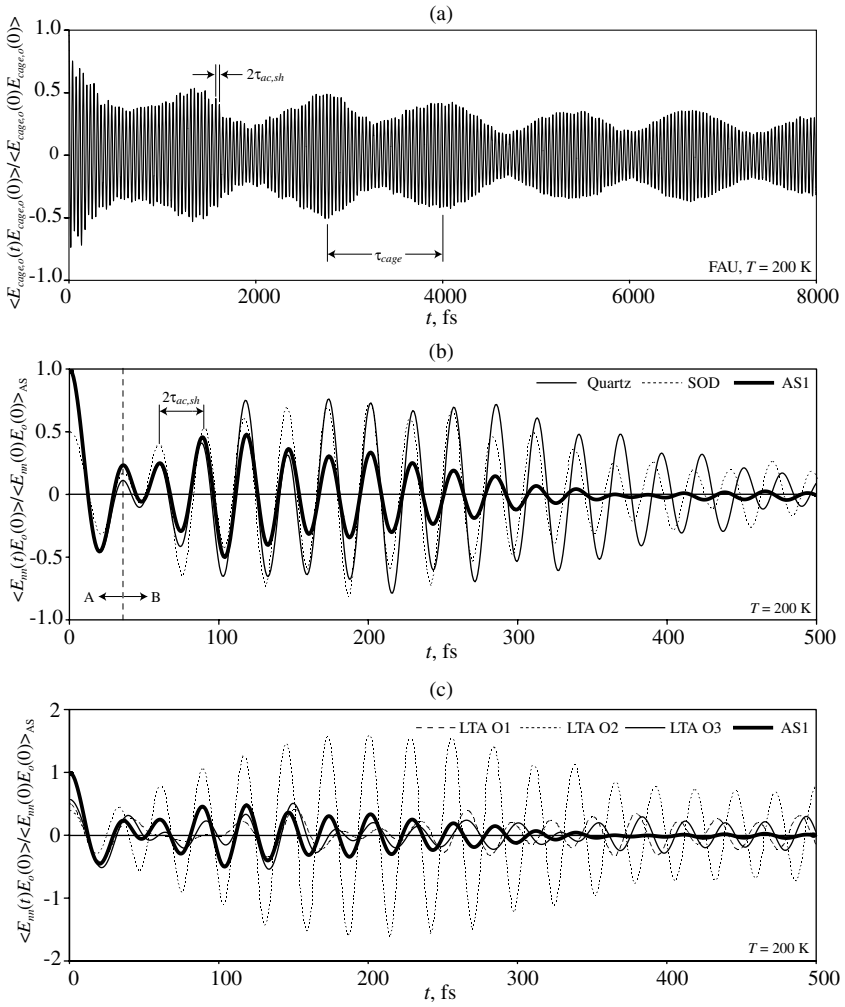

Fig. 6. (a) FAU sodalite cage energy autocorrelation function; (b) and (c) silicon–silicon nearest neighbor energy correlation functions. Note the different vertical scales in the two parts. The correlations are normalized against the $t = 0$ amorphous silica value. In all parts of the figure, the energy data correspond to deviations from the mean values.

against the zero-time amorphous silica value. The energy correlation contains three parts. There is an initial intra-tetrahedron portion [*A* in Fig. 6(b)], followed by a period over which adjoining tetrahedra come into phase and subsequently uncorrelate [*B* in Fig. 6(b)]. The third region (not shown) is a result of the periodic boundary conditions, and represents energy that has passed through the simulation cell and returned to its origin. The peaks in the correlations are separated by $2\tau_{ac,sh}$ (the time needed for energy to go across two Si–O bonds). The structures are distinguished by the second regime.

The results for quartz, SOD, and the amorphous silica phase are shown in Fig. 6(b). Consider the amorphous phase, where the absence of long range order prevents any significant coherence from developing, as a basis for comparison. In the quartz structure, the second regime contains a plateau. This allows coherence to develop between many subsequent tetrahedra, facilitating the flow of heat and resulting in a high thermal conductivity. In SOD, there is also an increased correlation compared to the amorphous phase, but it does not last as long as that in quartz. The thermal conductivity falls below the quartz value, but above the amorphous result.

The results for LTA are shown in Fig. 6(c), along with the amorphous silica curve. The O1 and O3 positions (see Fig. 7) show a lower correlation than that of the amorphous structure over much of the time up to 200 fs. The O2 position shows an even larger correlation than that in quartz. In particular, the O1 correlation is close to zero in a number of regions. This is the oxygen associated with the bridge between the sodalite cages, indicating that it is very difficult for energy to flow along

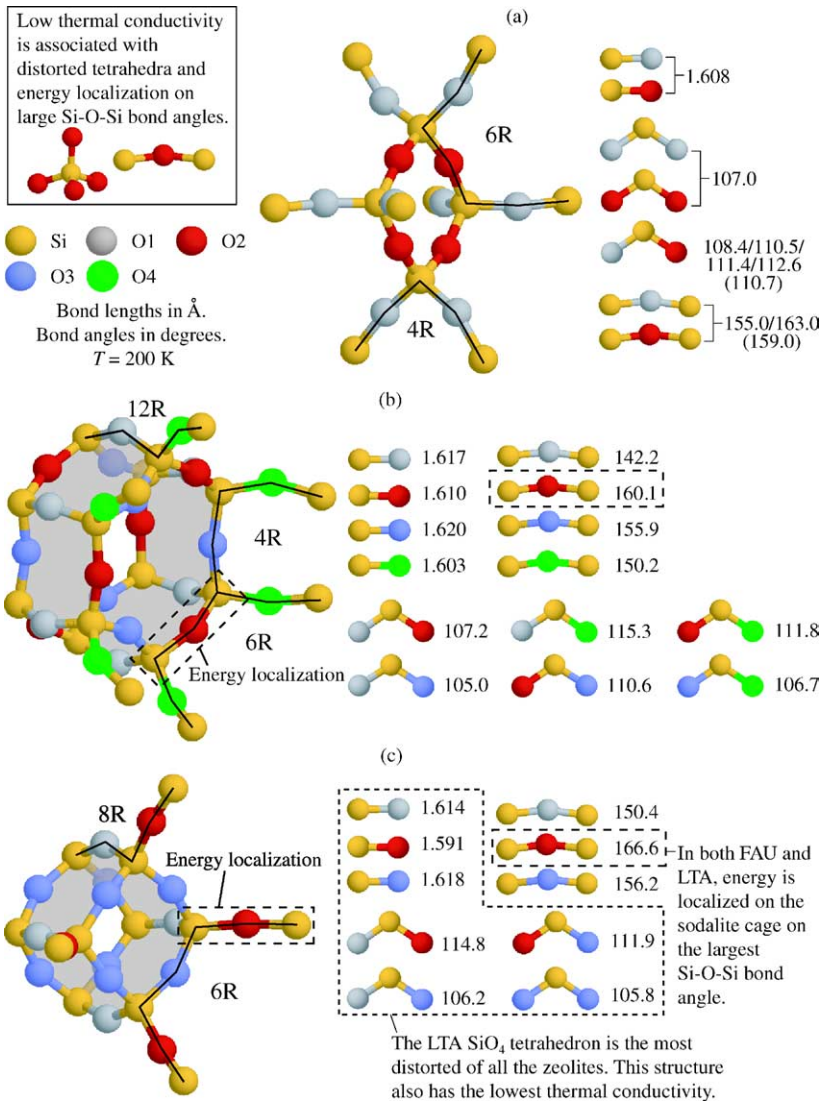

Fig. 7. Structure of the three zeolites near the linking of their sodalite cages. Bond lengths and angles correspond to $T = 200$ K: (a) SOD; (b) FAU, and (c) LTA.

that path. The only option for the energy is to flow over the O2 or O3 atoms, the latter of which also offers a strong resistance to the energy flow. This leads to a strong localization of energy on the Si–O2–Si subunit. Energy will go back and forth over the O2 atoms, and strong long range coherence cannot be established. Accordingly, LTA is found to have the lowest thermal conductivity and $k_{ac,lg}$ of all the crystals. For the FAU structure, a similar behavior is observed for the Si-Si correlations, although not as severe. In this case, it is also the bridge oxygens that most restrict the flow of heat, leading to a localization of energy on the sodalite cage. FAU has the second lowest thermal conductivity and $k_{ac,lg}$.

Having identified what is happening to inhibit the propagation of acoustic phonons over long length scales, the question turns to how the crystal structures bring about this effect. To do so, static and dynamic atomic level descriptions of the crystals will be considered.

In Fig. 7, the structure of each of the zeolites around the connections between sodalite cages is shown, along with the equilibrium bond lengths and angles. Portions of SBUs are marked, as is the location where the energy localization takes place in FAU and LTA. For the SOD structure, the equilibrium system is metastable, and oscillates between two equivalent states which have slightly distorted sodalite cages. The numbers in brackets below the data corresponding to the Si-O1–Si/Si–O2–

Si and O1–Si–O2 bond angles are time averaged values, while the given data correspond to the values within one of the two states.

While the zeolites considered are distinguishable based on their unit cells, they can also be characterized by the local environment of each silicon atom. In Table 5, the mean deviation of the angles in a tetrahedron for each of the zeolites is given based on the average bond angles at a temperature of 200 K. Also included is the equilibrium spread of the bond lengths at this temperature. As the distortion increases, the value of $k_{ac,lg}$ decreases. As quartz and amorphous silica do not contain sodalite cages, they are not included in this analysis. Murashov [45] has investigated the thermal conductivity of LTA when some of the silicon atoms are replaced with other species. These replacements lead to a distortion of the tetrahedra (which is shown using radial distribution functions) and an accompanying decrease in the thermal conductivity. Here, we see that the crystal structure itself can have the same effect.

In the FAU and LTA structures, the energy localization takes place on a Si–O–Si bond on the 6R SBU. In SOD, the overlapping of the cages makes the corresponding bond a part of another cage link, preventing the localization from developing. This is the largest Si–O–Si bond in each of the FAU and LTA structures, with values of 160.1° and 166.6°, respectively. This suggests that large bond angles may contribute to the localization. In quartz, all the Si–O–Si bonds have a magnitude of 148.2°, consistent with this argument.

The equilibrium geometries give the static properties of the lattices. The dynamics can be investigated by calculating root mean square (rms) displacements of individual atoms. In Fig. 8, the total and direction dependent

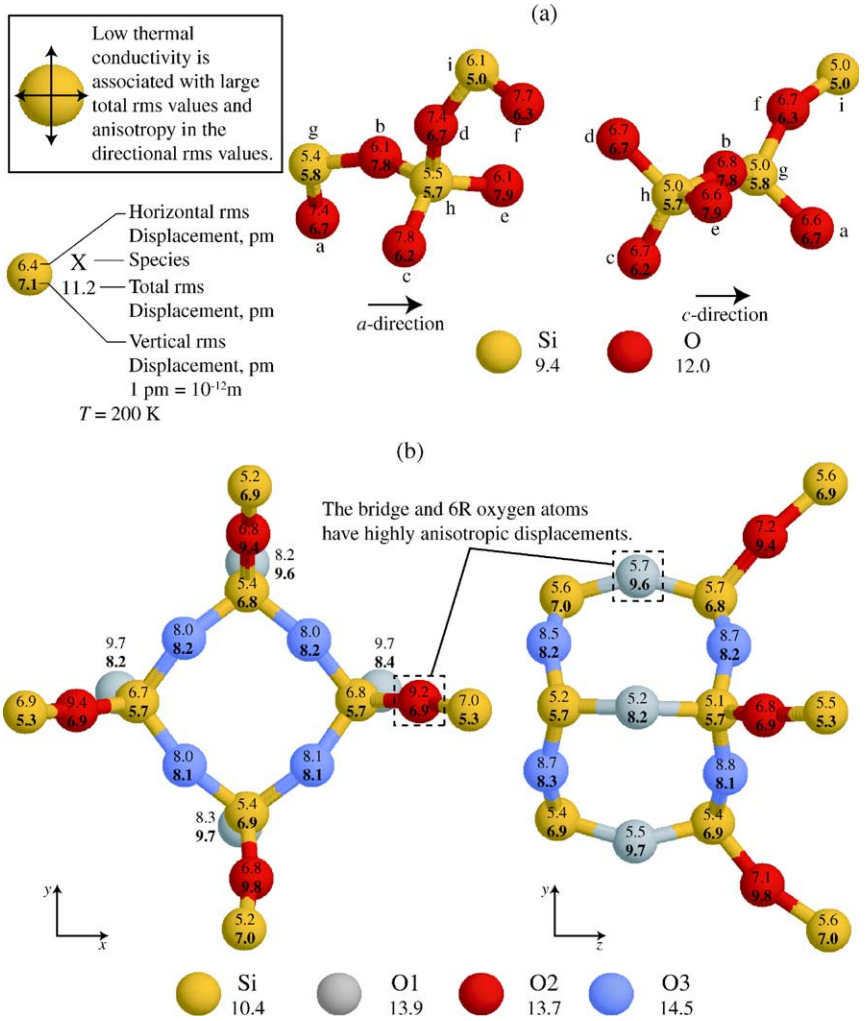

Fig. 8. Total and direction dependent rms displacements for the atoms in the quartz and LTA structures at $T = 200$ K: (a) quartz and (b) LTA.

rms displacements are shown for quartz and LTA at a temperature of 200 K. The oxygen atoms in LTA are distinguished using the same color scheme as in Fig. 7. In quartz, the two views are linked through the atom identifiers '*a*' to '*i*'. The number below the species identifier is the total rms displacement in picometers. There are two numbers associated with each atom in the structure. The top number is the horizontal rms displacement for the orientation shown, and the bottom number is the vertical rms displacement. Two orthogonal views are shown to give the full three dimensional description.

In general, smaller atomic motions correspond to less anharmonic interactions and an expected higher thermal conductivity. The total rms of the atoms in LTA are larger than those in quartz, and LTA has a lower thermal conductivity, consistent with this description. The anisotropies in the directional rms values for LTA are significantly larger than those in quartz. This increased anisotropy is consistent with idea of local distortion leading to an inhibition of the development of long length scale correlations, and a lower $k_{ac,lg}$.

5. Summary

The thermal conductivity decomposition introduced in Part I for LJ argon has been extended to model silica crystals. As shown in Fig. 4, the optical phonons present due to the multi-atom unit cells make a non-negligible contribution to the thermal conductivity when the total value is 10 W/m K or lower. The full decomposition is suitable for the analysis of any dielectric crystal.

The range of silica-based crystals available has allowed for insight to be gained into how heat is transferred in these materials. Two mechanisms have been identified. The first, which is short range and linked to optical phonons and short wavelength acoustic phonons, is related to the geometry of the crystal structure. The resulting thermal conductivity, shown in Fig. 5(b), is temperature independent, and has been interpreted as a minimum value for the crystal phase. This limiting value is different from that predicted by available models based on a disordered structure. The second mechanism corresponds to the long time propagation of acoustic phonons within a crystal. It accounts for the temperature dependence and majority of the magnitude of the thermal conductivity. The establishment of long time scale behavior is linked to the smallest scales of the crystal structure. Distortion of the SiO_4 tetrahedra can result in an inhibition of long range modes and a spatial localization of energy on the sodalite cages, as found in the zeolites (see Figs. 6–8).

In the design of new porous crystals with desired thermal properties, a number of guidelines can thus be suggested. When comparing to a similar dense phase, the thermal conductivity of the porous crystal will be lower due to the possibilities for energy localization on the cages. The amount of reduction is dependent on the structure of the cage, and to what extent it distorts small scale features such as bond lengths and angles. The size of the cage is not necessarily the limiting factor. This localization is able to almost completely eliminate long range coherence from developing in the crystals, as seen in LTA. However, there is an additional limit imposed by the crystal structure, related to the spatial distribution of atoms. The limiting thermal conductivity is related to the number of independent paths that energy can flow through from a given atom. The fewer the paths, the lower the thermal conductivity. This is not directly a density effect, but is related to the coordination of the atoms.

Acknowledgements

This work has been supported by the U.S. Department of Energy, Office of Basic Energy Sciences under grant DE-FG02-00ER45851, and the Natural Sciences and Engineering Research Council of Canada (AJHM).

References

[1] A. Dyer, An Introduction to Zeolite Molecular Sieves, Wiley, Chichester, 1988 (Chapter 1).
[2] G.S. Nolas, D.T. Morelli, T.M. Tritt, Skutterudites: A phonon-glass-electron crystal approach to advanced thermoelectric energy conversion applications, Annu. Rev. Mater. Sci. 29 (1999) 86–116.
[3] L. Forro, L. Mihaly, Electronic properties of doped fullerenes, Rep. Progress Phys. 64 (2001) 649–699.
[4] H. Li, M. Eddaoudi, M. O'Keeffe, O.M. Yaghi, Design and synthesis of an exceptionally stable and highly porous metal–organic framework, Nature 402 (1999) 276–279.
[5] M. Eddaoudi, J. Kim, N. Rosi, D. Vodak, J. Wachter, M. O'Keeffe, O.M. Yaghi, Systematic design of pore size and functionality in isoreticular MOFs and their application in methane storage, Science 295 (2002) 469–472.
[6] R.C. Yu, N. Tea, M.B. Salamon, D. Lorents, R. Malhotra, Thermal conductivity of single crystal C_{60}, Phys. Rev. Lett. 68 (1992) 2050–2053.
[7] B. Wolfing, C. Kloc, J. Teubner, E. Bucher, High performance thermoelectric Tl_9BiTe_6 with extremely low thermal conductivity, Phys. Rev. Lett. 86 (2001) 4350–4353.
[8] M. O'Keeffe, M. Eddaoudi, H. Li, T. Reineke, O.M. Yaghi, Frameworks for extended solids: geometrical design principles, J. Solid State Chem. 152 (2000) 3–20.
[9] M. Eddaoudi, D.B. Moler, H. Li, B. Chen, T.M. Reineke, M. O'Keeffe, O.M. Yaghi, Modular chemistry: Secondary building units as a basis for the design of highly porous and robust metal–organic carboxylate frameworks, Accounts Chem. Res. 34 (2001) 319–330.

[10] J.M. Newsam, The zeolite cage structure, Science 231 (1986) 1093–1099.
[11] J.M. Thomas, The Balkerian lecture, 1990: new microcrystalline catalysts, Philos. Trans. Phys. Sci. Eng. 333 (1990) 173–207.
[12] P. Demontis, G.B. Suffritti, Structure and dynamics of zeolites investigated by molecular dynamics, Chem. Rev. 97 (1997) 2845–2878.
[13] M. Omini, A. Sparavigna, Beyond the isotropic-model approximation in the theory of thermal conductivity, Phys. Rev. B 53 (1996) 9064–9073.
[14] A. Sparavigna, Influence of isotope scattering on the thermal conductivity of diamond, Phys. Rev. B 65 (2002) 064305.
[15] A.J.H. McGaughey, M. Kaviany, Quantitative validation of the single mode relaxation time phonon thermal conductivity model, Phys. Rev. B (submitted).
[16] A.J.H. McGaughey, M. Kaviany, Thermal conductivity decomposition and analysis using molecular dynamics simulations. Part I. Lennard-Jones argon, previous paper.
[17] R.W.G. Wyckoff, Crystal Structures, Interscience, New York, 1963, pp. 312–312 (Volume 1), pp. 402, 407, 430 (Volume 4).
[18] B.W.H. van Beest, G.J. Kramer, R.A. van Santen, Force fields for silicas and aluminophosphates based on *ab initio* calculations, Phys. Rev. Lett. 64 (1990) 1955–1958.
[19] G.J. Kramer, N.P. Farragher, B.W.H. van Beest, R.A. van Santen, Interatomic force fields for silicas, aluminophosphates, and zeolites: Derivation based on *ab initio* calculations, Phys. Rev. B 43 (1991) 5068–5080.
[20] J.S. Tse, D.D. Klug, The structure and dynamics of silica polymorphs using a two-body effective potential model, J. Chem. Phys. 95 (1991) 9176–9185.
[21] D. Wolf, P. Keblinski, S.R. Phillpot, J. Eggebrecht, Exact method for the simulation of Coulombic systems by spherically truncated, pairwise r^{-1} summation, J. Chem. Phys. 110 (1999) 8254–8282.
[22] Z.A. Rycerz, P.W.M. Jacobs, Ewald summation in the molecular dynamics simulations of large ionic systems: The cohesive energy, Molec. Simulat. 8 (1992) 197–213.
[23] Z.A. Rycerz, Calculation of the Coulombic interactions in condensed matter simulation, Molec. Simulat. 9 (1992) 327–349.
[24] P. Demontis, S. Spanu, G.B. Suffritti, Application of the Wolf method for the evaluation of Coulombic interactions in complex condensed matter systems: aluminosilicates and water, J. Chem. Phys. 114 (2001) 7980–7988.
[25] Y. Guissani, B. Guillot, A numerical investigation of the liquid-vapor coexistence curve of silica, J. Chem. Phys. 104 (1996) 7633–7644.
[26] E. Demiralp, N.T. Huff, T. Cagin, W.A. Goddard III, Factors affecting molecular dynamics simulated vitreous silica structures, in: M.K. Choudhary, N.T. Huff, C.H. Drummond III (Eds.), Proceedings of the XVIII International Congress on Glass, San Francisco, CA, 1998, pp. 61–66.
[27] M. Kaviany, Principles of Heat Transfer, Wiley, New York, 2002, p. 929.
[28] P. Jund, personal communication.
[29] S.N. Taraskin, S.R. Elliot, The dispersion of vibrational excitations in vitreous silica, Philos. Mag. B 77 (1998) 403–420.
[30] P. Jund, R. Jullien, Molecular-dynamics calculation of the thermal conductivity of vitreous silica, Phys. Rev. B 59 (1999) 13707–13711.
[31] D.A. McQuarrie, Statistical Mechanics, University Science Books, Sausalito, 2000, pp. 520–521.
[32] J. Li, L. Porter, S. Yip, Atomistic modeling of finite-temperature properties of crystalline β-SiC. II. Thermal conductivity and effects of point defects, J. Nucl. Mater. 255 (1998) 139–152.
[33] H. Kaburaki, J. Li, S. Yip, Thermal conductivity of solid argon by classical molecular dynamics, Mater. Res. Soc. Symp. Proc. 538 (1998) 503–508.
[34] J. Li, Modeling microstructural effects on deformation resistance and thermal conductivity, Ph.D. Thesis, Massachusetts Institute of Technology, Cambridge, MA, 2000.
[35] J. Che, T. Cagin, W. Deng, W.A. Goddard III, Thermal conductivity of diamond and related materials from molecular dynamics simulations, J. Chem. Phys. 113 (2000) 6888–6900.
[36] J. Dong, O.F. Sankey, C.W. Myles, Theoretical study of lattice thermal conductivity in Ge framework semiconductors, Phys. Rev. Lett. 86 (2001) 2361–2364.
[37] P. Bornhauser, D. Bougeard, Intensities of the vibrational spectra of siliceous zeolites by molecular dynamics calculations. I. Infrared spectra, J. Phys. Chem. B 105 (2001) 36–41.
[38] K.S. Smirnov, D. Bougeard, Computer modeling of the infrared spectra of zeolite catalysts, Catal. Today 70 (2001) 243–253.
[39] A.J.M. de Man, R.A. van Santen, The relationship between zeolite framework structure and vibrational spectra, Zeolites 12 (1992) 269–279.
[40] K.A. Iyer, S.J. Singer, Local-mode analysis of comlex zeolite vibrations: Sodalite, J. Phys. Chem. 98 (1994) 12670–12678.
[41] K.A. Iyer, S.J. Singer, Local-mode analysis of comlex zeolite vibrations: Zeolite-A, J. Phys. Chem. 98 (1994) 12679–12686.
[42] D.G. Cahill, R.O. Pohl, Heat flow and lattice vibrations in glasses, Solid State Commun. 70 (1989) 927–930.
[43] D.G. Cahill, S.K. Watson, R.O. Pohl, Lower limit to thermal conductivity of disordered crystals, Phys. Rev. B 46 (1992) 6131–6140.
[44] Y. Touloukian, Thermophysical Properties of Matter, Vol. 2, Plenum, New York, 1970, pp. 182, 193.
[45] V.V. Murashov, Thermal conductivity of model zeolites: Molecular dynamics study, J. Phys.: Cond. Matter 11 (1999) 1261–1271.
[46] A. Griesinger, K. Spindler, E. Hahne, Measurements and theoretical modelling of the effective thermal conductivity of zeolites, Int. J. Heat Mass Transfer 42 (1999) 4363–4374.
[47] C. Oligschleger, J.C. Schon, Simulation of thermal conductivity and heat transport in solids, Phys. Rev. B 59 (1999) 4125–4133.
[48] J. Michalski, Thermal conductivity of amorphous solids above the plateau: molecular-dynamics study, Phys. Rev. B 45 (1992) 7054–7065.
[49] R.H.H. Poetzsch, H. Bottger, Interplay of disorder and anharmonicity in heat conduction: molecular-dynamics study, Phys. Rev. B 50 (1994) 15757–15763.

[50] P.B. Allen, J.L. Feldman, J. Fabian, F. Wooten, Diffusons, locons and propagons: Character of atomic vibrations in amorphous Si, Philos. Mag. B 79 (1999) 1715–1731.
[51] A. Majumdar, Microscale energy transport in solids, in: C.-L. Tien, A. Majumdar, F.M. Gerner (Eds.), Microscale Energy Transport, Taylor and Francis, Washington, 1998, p. 72.
[52] Kaviany, op. cit., p. 179.
[53] M. O'Keeffe, S.T. Hyde, Vertex symbols for zeolite nets, Zeolites 19 (1997) 370–374.
[54] P.K. Schelling, S.R. Phillpot, Mechanism of thermal transport in zirconia and yttria-stabilized zirconia by molecular-dynamics simulation, J. Am. Ceram. Soc. 84 (2001) 2997–3007.